RSC Advances

PAPER

View Article Online
View Journal | View Issue

Cite this: *RSC Adv.*, 2017, **7**, 5898

One step synthesis of Ni/Ni(OH)$_2$ nano sheets (NSs) and their application in asymmetric supercapacitors†

Sivasankara Rao Ede,[ab] S. Anantharaj,[ab] K. T. Kumaran,[b] Soumyaranjan Mishra[b] and Subrata Kundu*[abc]

Ni(OH)$_2$ is a useful electrode material for electrochemical capacitors, due to its high theoretical specific capacitance and low cost, but its application has been limited by poor electrical conductivity. Hence, we fabricated Ni(OH)$_2$ nano sheets (NSs) with nickel metal NPs *via* the hydrothermal partial reduction of Ni(II) salt by ethanol in basic medium. The significance of the basic medium (presence of KOH) and other reaction parameters and the mechanism for the formation of Ni/Ni(OH)$_2$ NSs are elaborated. The Ni/Ni(OH)$_2$ NSs have been used as a positive electrode in an asymmetric supercapacitor (ASC) with a larger voltage window using the activated carbon (AC) as a negative electrode, which resulted in high energy and power densities. By optimizing the mass ratio between AC and Ni/Ni(OH)$_2$ NSs in the fabrication of electrodes, we found a maximum specific capacitance (C_S) of 62 F g^{-1} at 2 mA cm^{-2} at a voltage of 1.65 V and observed the maximum energy and power densities of 23.45 W h kg^{-1} and 4598 W kg^{-1}, respectively. The galvanostatic charge–discharge study shows high capacity retention up to 90%, even after 6000 consecutive cycles, which is a noteworthy achievement, considering the ASCs. Moreover, we believe that the presence of nickel metal in Ni/Ni(OH)$_2$ NSs helped to reduce the charge transfer resistance (R_{CT}), which resulted in better performance. These results certainly demonstrate that such Ni/Ni(OH)$_2$ NSs with Ni metal NPs are promising materials for the construction of next generation aqueous ASCs with higher specific capacitance. The synthesis procedure can be applied to other transition metals to synthesize their metal/metal hydroxide composites and enhance their conductive nature, instead of using conductive substrates.

Received 10th November 2016
Accepted 16th December 2016

DOI: 10.1039/c6ra26584g

www.rsc.org/advances

Introduction

Supercapacitors and fuel cells are alternative energy storage systems to batteries. Supercapacitors are the contemporary generation of energy storage systems, due to their fast rates of charging/discharging, high rate capability, high power density, and outstanding cycle stability.[1–5] Nowadays, supercapacitors supersede batteries in an array of applications. However, supercapacitors are still behind batteries in energy storage applications, due to their relatively poor energy densities.[6] Intense efforts need to be invested in improving the energy and power densities of supercapacitors to establish them as an alternate means of power supply.[7,8] Fabricating advanced supercapacitor devices that would give comparable energy densities and at the same time retain high power density and cycle life is therefore quite important.[9] This can be done either by increasing the capacitance or by extending the operating potential window.[10,11] One of the most commonly practiced ways of augmenting cell voltage nowadays is the application of organic electrolytes that are known for wider potential windows with improved electrochemical stability, compared to aqueous systems. However, problems arise due to their lower conductivity, toxicity and cost effectiveness, as compared to aqueous electrolytes. The low conductivity greatly reduces specific capacitance and unfortunately, spikes up the equivalent series resistance (ESR), which in turn prevents high specific power density. Hence, aqueous electrolytes are among the best options to develop cost-effective and ecofriendly supercapacitors.

Low-cost transition-metal oxide supercapacitor electrode materials in aqueous electrolytes are applied as symmetric and asymmetric capacitors, owing to their enhanced specific capacitance, although they possess a narrow potential window of 1 V in symmetric supercapacitors.[12] Recently, Yamauchi *et al.*

[a]*Academy of Scientific and Innovative Research (AcSIR), CSIR-Central Electrochemical Research Institute (CSIR-CECRI) Campus, New Delhi, India. E-mail: skundu@cecri.res.in; kundu.subrata@gmail.com; Fax: +91-4565-227651; Tel: +91-4565-241487*

[b]*Electrochemical Materials Science (ECMS) Division, CSIR-Central Electrochemical Research Institute (CECRI), Karaikudi-630006, Tamil Nadu, India*

[c]*Department of Materials Science and Mechanical Engineering, Texas A&M University, College Station, Texas, TX-77843, USA*

† Electronic supplementary information (ESI) available: Details on instrument specifications, sample preparation for various analyses, figures related to XPS analysis, figures and tables related to electrochemical studies are provided. See DOI: 10.1039/c6ra26584g

demonstrated high cyclic stability, high specific energy and power densities using metal organic frameworks (MOF)[13] and nano porous carbon derived from MOF[14] in symmetric supercapacitors. However, due to the narrow potential window of symmetric supercapacitors, energy and power densities cannot be optimized to higher values as required in industries; it is therefore desirable to fabricate supercapacitors with two different electrodes, where one could be the electrochemical double layer capacitor (EDLC) and the other could be a pseudocapacitor. The asymmetric set-up greatly increases the potential window and also the specific capacitance, energy and power densities, and the dual electrode set-up may be a combination of two distinct transition metal oxide electrodes,[12,15] or a combination of an activated carbon and metal oxide electrode,[11,12,15–18] or that of a conducting polymer and an oxide electrode.[19] Several electroactive materials, such as $Ni(OH)_2$,[20] MnO_2,[21] V_2O_5,[22] CoO,[23] Fe_2O_3,[24] $MnWO_4$,[25] $NiWO_4$,[26] $ZnWO_4$ [27] and Nb_2O_5 [28] have been reported as supercapacitor materials, amongst which $Ni(OH)_2$ is gifted with high theoretical specific capacitance (2082 F g^{-1}) and is often applied as the discharged-state material in the electrodes, owing to its stability in strong alkaline electrolyte, which is due to the short diffusion path length of the electrolyte, as well as high reversibility and excellent rate capability when oxidized to NiOOH.[29] Nevertheless, besides having high specific capacitance, it is a poor electronic conductor, a factor that limits its ability to reach the theoretical capacitance on its own.

So far, intense efforts have been made to decrease ESR and R_{CT} by increasing the conductive nature of the transition metal oxides/hydroxides by synthesizing and fabricating these active materials on conductive substrates through various methods.[30–33] Some of the significant reports are highlighted below. Yu *et al.* synthesized $NiCo_2O_4$ nano needles on graphene-nickel foam (GNF) by a two-step approach;[30] Ho *et al.* synthesized MnO_2 electrochemically deposited on stainless steel;[31] Gong *et al.* synthesized nickel cobalt hydroxide microspheres electrodeposited on nickel cobaltite nanowires grown on Ni foam by a two step method,[32] and cobalt monoxide nickel hydroxide nitrate composite was synthesized on nickel foam by a two-step hydrothermal route by Guan *et al.*[33] All of the above methods employed more than one step to synthesize the desired active material. Moreover, the control over the loading of active materials involved in the electrochemical reactions by these methods was very poor. Another major pitfall is the conversion of the nickel foam surface into nickel oxide during hydrothermal or electrodeposition, thus increasing the resistance of the nickel foam, which will directly affect the capacitive performance of pristine material. In order to avoid all these pitfalls, we have synthesized $Ni/Ni(OH)_2$ NSs by a facile one-step hydrothermal synthesis with the aid of oleylamine and ethanol as a reducing agent in basic medium, for the first time. The maximum specific capacitances of 536 F g^{-1} $Ni/Ni(OH)_2$ NSs by cyclic voltammetry (CV) at a scan rate of 5 mV s^{-1} and 450 F g^{-1} by chronopotentiometry at a current density of 1 mA cm^{-2} were achieved in 1 M KOH aqueous solution. Our optimized ASC showed a specific capacitance of 62 F g^{-1} at 2 mA cm^{-2} and a maximum energy density of 23.45 W h kg^{-1}, without sacrificing the power density. Moreover, the fabricated material also showed a good long-term cycling stability as derived from galvanostatic charge–discharge (GCD) measurements, where only a 10% decrease from its initial specific capacitance was observed, even after 6000 cycles. These outcomes suggest that such $Ni/Ni(OH)_2$ NSs will be promising materials for the next generation of high-performance ASCs. For comparison, we synthesized $NiO/Ni(OH)_2$ NSs by varying the concentration of KOH and studied the electrochemical properties along with $Ni/Ni(OH)_2$ NSs for a three electrode system.

Experimental section

Reagents and instruments

All the chemicals used in this present work were analytical reagent (AR) grade. The nickel(II) acetate hexahydrate ($Ni(Ac)_2 \cdot 6H_2O$), oleylamine, potassium hydroxide (KOH) and cyclohexane were procured from Sigma-Aldrich and used without any further purification. Ethanol was purchased from SRL, India. Polyvinylidene fluoride (PVDF), *N*-methyl-2-pyrrolidinone (NMP), carbon black, activated carbon and nickel foam were obtained from Alfa Aesar and used as received. De-ionized (DI) water was used for the entire synthesis and application purposes. The synthesized $Ni/Ni(OH)_2$ and $NiO/Ni(OH)_2$ NSs were characterized using several techniques, such as XRD, TEM, and XPS, and electrochemical studies were done through an electrochemical work station, CHI-6084C. Instrument specifications and sample preparation for various characterizations are provided in the online ESI.†

Hydrothermal synthesis of $Ni/Ni(OH)_2$ and $NiO/Ni(OH)_2$ NS arrays

For a typical synthesis of $Ni/Ni(OH)_2$ NSs, 0.248 g of nickel(II) acetate hexahydrate were taken with 20 mL of ethanol and 1.5 mL of oleylamine and subjected to mechanical stirring for 20 min. Further, 1 mL of oleylamine dispersed in 10 mL of ethanol was swiftly added, followed by 2 mL of KOH (0.1 M) and the stirring was continued for another 30 min in order to homogenize the whole reaction mixture. The entire contents were then transferred to a Teflon-lined autoclave of 50 mL volume capacity. The sealed autoclave was subjected to constant heating at 160 °C for 24 h. The blackish precipitate obtained after the solvothermal treatment was separated and washed a couple of times with ethanol and cyclohexane to expel the excess organics in the synthesized material. Finally, the blackish powder obtained was dried in a vacuum oven at 60 °C for 2 h. The same synthesis procedure was followed for the synthesis of $NiO/Ni(OH)_2$ NSs, with the exclusion of the addition of KOH. The obtained greenish precipitate was separated after the solvothermal treatment and washed a couple of times with ethanol and cyclohexane. The details of the concentrations of the reagents used and pH of the synthesis of $Ni/Ni(OH)_2$ and $NiO/Ni(OH)_2$ NSs are listed in Table 1. The overall synthesis and visible changes at various stages of the synthesis are schematically illustrated in Scheme 1. The synthesized $Ni/Ni(OH)_2$ and $NiO/Ni(OH)_2$ NSs were further characterized using X-ray

Table 1 The details of concentrations of the reagent used, and their pH values, for the synthesis of $Ni/Ni(OH)_2$ and $NiO/Ni(OH)_2$ NSs

	Final concentration (M)		pH values	
Reagents	$Ni/Ni(OH)_2$ NS	$NiO/Ni(OH)_2$ NS	$Ni/Ni(OH)_2$ NS	$NiO/Ni(OH)_2$ NS
Ni(II) acetate	27×10^{-3}	27×10^{-3}	6.4	6.4
KOH	6×10^{-3}	—	13.0	—
Oleylamine	2.1×10^{-2}	2.1×10^{-2}	11.0	11.0
Mixture of all reagents	—	—	9.5	8.4

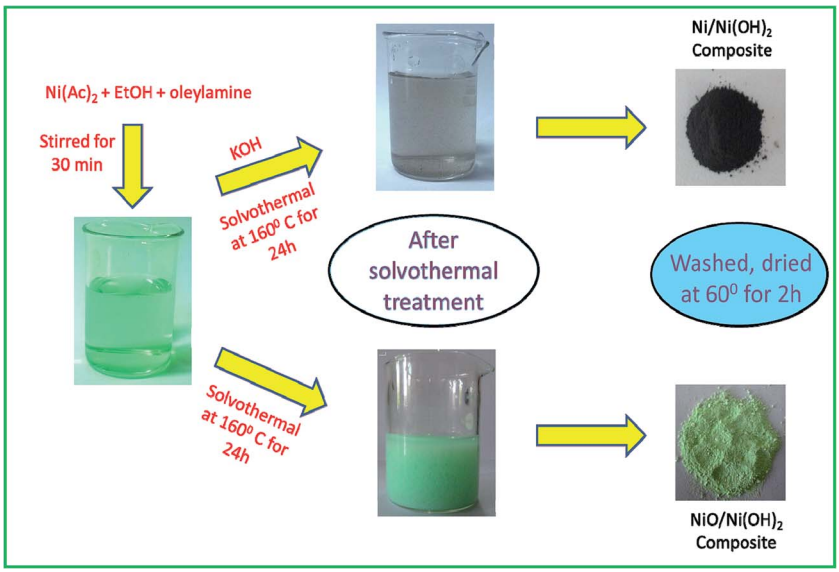

Scheme 1 Schematic representation of $Ni/Ni(OH)_2$ and $NiO/Ni(OH)_2$ NSs synthesis, and visible observations.

diffraction (XRD), transmission electron microscope (TEM) and X-ray photoelectron spectroscopy (XPS) analyses (Scheme 2).

Fabrication of electrodes and electrochemical calculations

The working electrode was prepared by mixing the electroactive material, acetylene black, and polyvinylidene fluoride (PVDF) in a mass ratio of 80 : 15 : 5 with *N*-methyl-2-pyrrolidone (NMP). About 2.4 mg of active material (excluding the mass of acetylene black and PVDF) of the as prepared homogenous slurry was coated on the nickel foam taken as the current collector (area = 1 cm × 1 cm), and dried at 120 °C for 12 h to evaporate the solvent. The conventional three electrode system with aqueous 1 M KOH electrolyte was used for obtaining electrochemical measurements. A platinum sheet and Ag/AgCl were used as the counter and reference electrodes, respectively. The electrochemical impedance spectroscopy (EIS) was carried out over the frequency range of 100 kHz to 0.01 Hz with an AC amplitude of 5 mV at open circuit potential. The specific capacitances of the electrodes were calculated from the CV and GCD curves of the three electrode system, according to the following equations:

Specific capacitance from CV curves

$$C_{sp} = \frac{\int i\mathrm{d}V}{vm\Delta V} \quad (1)$$

Specific capacitance from GCD curves

$$C_{sp} = \frac{I\Delta t}{m\Delta V} \quad (2)$$

Energy density

$$E = 1/(2 \times 3.6) \times C_{sp}\Delta V^2 \text{ (W h kg}^{-1}\text{)} \quad (3)$$

Power density

$$P = (3600 \times E)/T \text{ (W kg}^{-1}\text{)} \quad (4)$$

where, $\int i\mathrm{d}V$ is the integrated area under the CV curve (A), v is the scan rate (mV s^{-1}), I is the discharge current (A), Δt is the discharge time (s), ΔV is the potential window (V), m is the mass of the electroactive material (g), C_{sp} is the specific capacitance (F g^{-1}) and T is the discharge time (s). The specific capacity of the ASC was optimized by amending the mass ratio between $Ni/Ni(OH)_2$ NSs and activated carbon (AC) by using the following equation:

$$\frac{m_+}{m_-} = \frac{C_-}{C_+} \times \frac{\Delta E_-}{\Delta E_+} \quad (5)$$

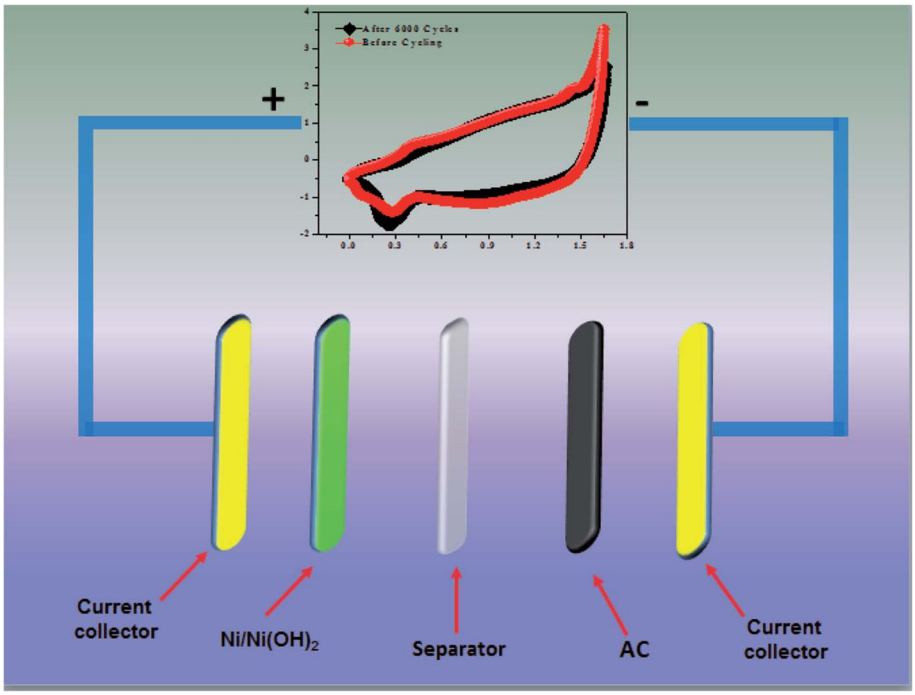

Scheme 2 Schematic representation of ASC.

where, m_+, m_-, C_+, C_-, ΔE_+ and ΔE_- are the masses, specific capacitances and potential windows of the three electrode configuration of the individual positive and negative electrodes, respectively. For ASC, the weight of the active material taken was 4 mg (1 : 4 ratio of Ni/Ni(OH)$_2$ and AC) excluding the mass of acetylene black and PVDF. A schematic representation of an ASC device is shown in Scheme 2.

Results and discussion

X-ray diffraction (XRD) studies

Fig. 1 shows the acquired XRD patterns of Ni/Ni(OH)$_2$ and NiO/Ni(OH)$_2$ NSs, which look similar to one another because they have Ni(OH)$_2$ in common. The peaks due to Ni(OH)$_2$ have been assigned in reference to the ICDD card number of 14-0117 for Ni(OH)$_2$ with diffraction planes (001), (100), (002), (110), (111), (200), (103) and (202). Fig. 1A shows XRD patterns of Ni also with three characteristic peaks at 44.6°, 51.9° and 76.5° (JCPDS 70-0989), which correspond to the (111), (200) and (220) diffraction planes, respectively. This is in accordance with the reported value for nickel metal nanoparticles.[34] From Fig. 1B we can observe that the NiO/Ni(OH)$_2$ NSs show four characteristic peaks of NiO at 37.2°, 43.2°, 62.8° and 76.5° (JCPDS 44-1159), corresponding to the (101), (012), (110) and (113) diffraction planes, respectively. The observed pattern is in good agreement with the earlier reports.[29]

X-ray photoelectron spectroscopic (XPS) studies

The X-ray photoelectron spectroscopic studies revealed the chemical nature of each element in the synthesized NSs. Fig. 2A shows the survey scan, which clearly depicts the presence of Ni, O and C at their corresponding binding energies in the synthesized NSs, which implies the absence of impurities. The presence of elements such as C is due to the substrate we used for XPS analysis (carbon tape). The high resolution scan of C 1s (Fig. S1C, online ESI section†) indicates the presence of sp^3 carbon at the binding energy of 284.5 eV, as expected. The Ni 2p XPS spectrum shows two major peaks with binding energies at 870.4 and 852.5 eV, corresponding to Ni 2p$_{1/2}$ and Ni 2p$_{3/2}$, respectively. The de-convoluted Ni 2p region shown in Fig. 2B, reveals the presence of nickel metal along with Ni(OH)$_2$. After deconvolution, the Ni 2p$_{1/2}$ spectrum shows peaks at 872.1 eV and 870.2 eV, and Ni 2p$_{3/2}$ shows peaks at 853.5 eV and 851.8 eV for Ni(OH)$_2$ and nickel metal, respectively. The high resolution scan of the Ni 2p state also contains two satellite peaks with considerable intensities, as observed in Fig. 2B. Similar types of satellite peaks were observed earlier by Grosvenor *et al.* for their study on nickel metal and oxides,[35] by Liu *et al.* in their study on NiNTAs@PPy[36] and by Xiao *et al.* for their study on MnO$_2$@3D-Ni nanodendrites.[37] Fig. 2C shows the high resolution scan of the O 1s state at a binding energy of 531.9 eV after deconvolution, showing two peaks that can be attributed to Ni–O–Ni and Ni–O–H at the binding energies of 531.6 and 530.8, respectively. The detailed XPS analysis supports the results obtained from the XRD analysis. For comparison, we have taken the XPS spectra for NiO/Ni(OH)$_2$ NSs, and the high resolution spectra of Ni 2p and O 1s are depicted as Fig. S1A and B (in the online ESI section†), respectively. From both figures, it is clearly revealed that the nickel exists as NiO and Ni(OH)$_2$ states in NiO/Ni(OH)$_2$ NSs, in accordance with the XRD results (Fig. 1B).

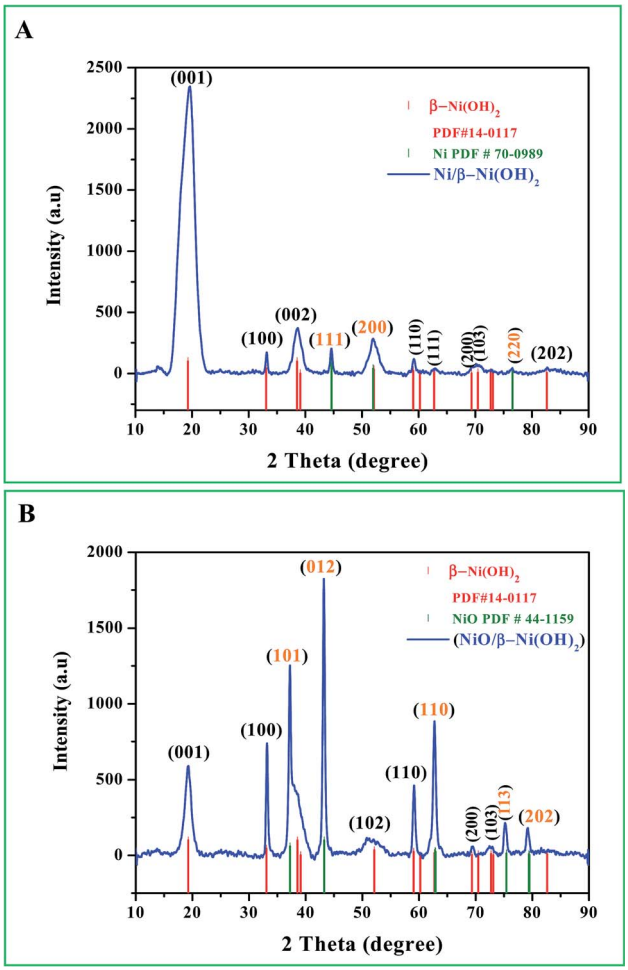

Fig. 1 (A and B) X-ray diffraction (XRD) patterns of the synthesized Ni/$Ni(OH)_2$ and NiO/$Ni(OH)_2$ NSs.

Topographical analysis and electron diffraction studies

The structure and morphology of the NSs were observed by transmission electron microscopy (TEM). Fig. 3A and B show the low and high magnification images of the as-prepared Ni/$Ni(OH)_2$ NSs. From Fig. 3B, the morphology seems to be of sheet-like architecture. It can also be observed that the sheets are interwoven with each other (Fig. 3A and B). Fig. 3C shows the corresponding SAED pattern of Ni/$Ni(OH)_2$. Careful observation of Fig. 3C shows the ring pattern of $Ni(OH)_2$ and the square pattern of Ni metal, and the diffraction spots that are identified in Fig. 3C are consistent with the XRD results (Fig. 1A). Fig. 3D and E show the low and high magnification images of the as-prepared NiO/$Ni(OH)_2$ NSs. Fig. 3F shows the corresponding SAED pattern of NiO/$Ni(OH)_2$, which is in accordance with the XRD results (Fig. 1A). Fig. 3G shows the high resolution TEM image of Ni/$Ni(OH)_2$ NSs, which reveals the corresponding crystal planes of Ni and $Ni(OH)_2$. This is in accordance with the earlier reports by Chen *et al.* for their study on polypyrrole shell@3D-Ni metal core[38] and by Liu *et al.* on their study on layered $Ni_xCo_{2x}(OH)_{6x}$@Ni material.[39]

Formation mechanism of Ni/$Ni(OH)_2$ NSs

Ni/$Ni(OH)_2$ NSs have been synthesized by the partial reduction of nickel(II) salt by using ethanol as a reducing agent in the presence of KOH at high pressure and at a temperature of 160 °C, *via* the hydrothermal method. We have monitored the role of various reaction parameters in the formation of Ni/$Ni(OH)_2$ NSs. It was observed that when we used KOH, it formed Ni/$Ni(OH)_2$ NSs arrays, whereas on keeping all reaction parameters fixed, except for the addition of KOH, it formed NiO/$Ni(OH)_2$. On the other hand, when we applied the solvothermal procedure (stirring and heating at 160 °C), keeping all other reaction parameters the same except pressure, we ended up with the formation of nickel hydroxide only, which strongly implies the role of KOH and pressure in the partial reduction of Ni(II) to Ni. Moreover, the appropriate combination of all reaction parameters is essential for the formation of Ni/$Ni(OH)_2$ NSs. Initially, ethanol reacts with KOH at high pressure and temperature and forms potassium ethoxide ($CH_2CH_3O^-K^+$), which is a moderate reducing agent and could partially reduce the nickel(II) salt into Ni metal, and the remaining Ni(II) ions are converted to $Ni(OH)_2$. A combination of these two simultaneous reactions lead to the formation of Ni/$Ni(OH)_2$ NSs. The corresponding chemical reactions for the formation of Ni/$Ni(OH)_2$ are given below. We have analyzed the role of KOH by measuring the pH of reaction mixtures at various stages during the synthesis of Ni/$Ni(OH)_2$ NSs. The pH of ethanol only was 6.4, 0.1 M KOH only was 13.0, oleylamine only was 11.0, the mixture of oleylamine and ethanol was 9.8, the mixture of ethanol and nickel(II) acetate was 6.4 and the mixture of all reagents was 9.5.

$$CH_3CH_2OH + KOH \xrightarrow[160\ ^\circ C,\ 24\ h]{\text{high pressure}} CH_3CH_2O^-K^+ + H_2O$$

$$Ni(CH_3COO)_2 + CH_3CH_2O^-K^+ \xrightarrow[160\ ^\circ C,\ 24\ h]{\text{high pressure}} Ni/Ni(OH)_2 + CH_3COO^-K^+$$

Overall reaction

$$Ni(CH_3COO)_2 + KOH + CH_3CH_2OH \xrightarrow[160\ ^\circ C,\ 24\ h]{\text{high pressure}} Ni/Ni(OH)_2$$

$$Ni(CH_3COO)_2 + CH_3CH_2OH \xrightarrow[160\ ^\circ C,\ 24\ h]{\text{high pressure}} NiO/Ni(OH)_2$$

The addition of a small amount of KOH not only adjusted the pH of the solution, but also played a crucial role in the partial reduction of the nickel precursor to nickel nanocomposite (Ni/$Ni(OH)_2$). This is in accordance with the previous reports by the Chen group and Roselina group.[40,41] Chen *et al.* observed that in the absence of NaOH, there was no formation of nickel NPs despite adjusting the pH (10.5) with a strong reducing agent like hydrazine hydrate. From

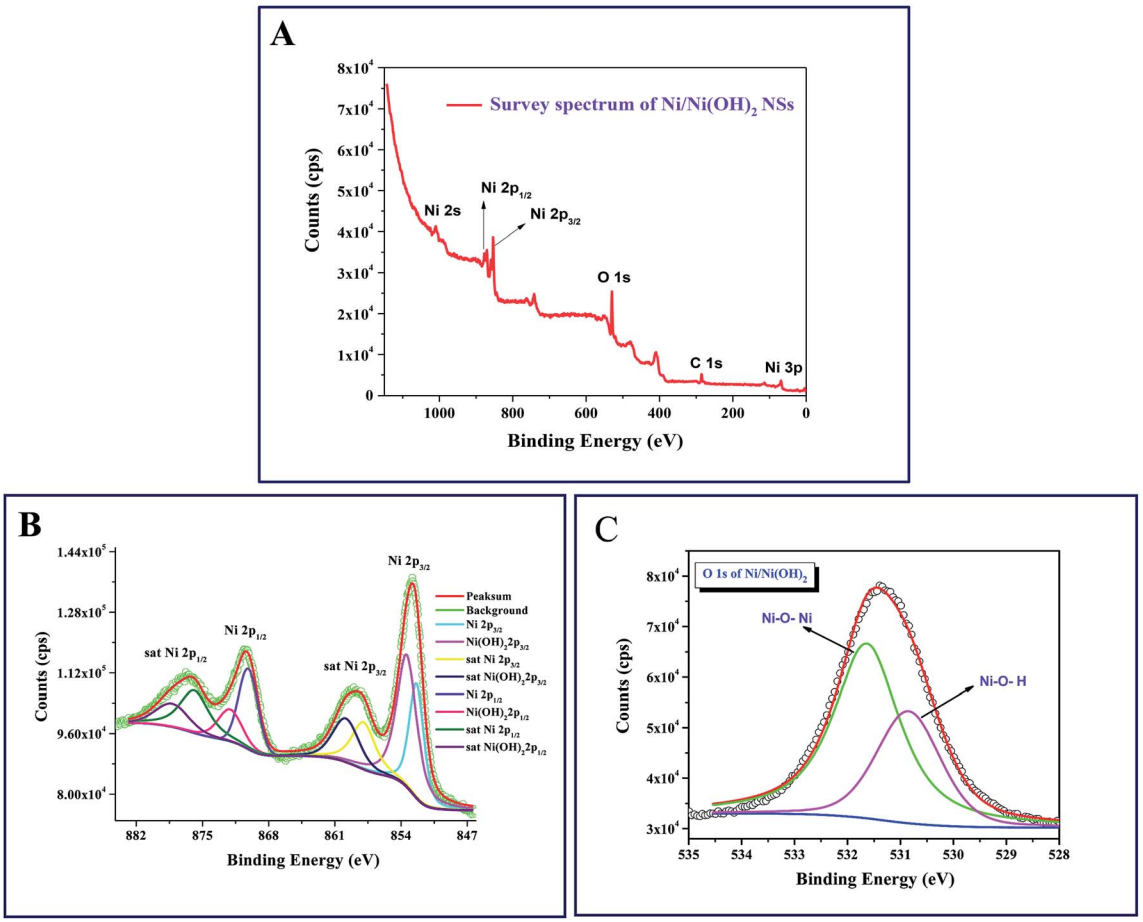

Fig. 2 (A) X-ray photoelectron spectra (XPS) of the survey of $Ni/Ni(OH)_2$ NS; (B) XPS of the Ni 2p state of Ni present in $Ni/Ni(OH)_2$ NSs. (C) XPS of O 1s state of O present in $Ni/Ni(OH)_2$ NSs.

this result, they concluded that the addition of NaOH might play a dual role in adjusting the pH as well as acting as a catalyst.[40] Likewise, the Roselina group noticed that in the absence of NaOH, the nickel precursor resulted in the formation of a complex mixture with hydrazine hydrate and nickel hydroxide instead of various nickel nanostructures.[41] It must be noted that there are several other reports for the reduction of metal salts to their corresponding metal nanoparticles (NPs) by the reducing activity of compounds that have hydroxyl groups, such as ethanol,[42] ascorbic acid,[43] PVA,[44] and 2,7-dihydroxynaphthalene (2,7-DHN)[45] that act as reducing agents. Ethanol has previously been used as a reducing agent for the formation of noble metal NPs such as Ag, Au, Pd, and Os. Ayyappan *et al.* reported ethanol as a reducing agent for the formation of metal NPs such as Ag, Au, Cu, Pd.[46] Likewise, Pal *et al.* reported the synthesis of Ag NPs using ethanol as a reducing agent and polyvinyl pyrrolidone (PVP) as a stabilizer.[47] Recently, our group reported the formation of Os NPs by the reduction of OsO_4 with ethanol by microwave heating.[48] Hence, we also believe that ethanol might acts as a reducing agent by the formation of potassium ethoxide at high pressure and temperature, which is responsible for the formation of $Ni/Ni(OH)_2$ NSs.

Three electrode system electrochemical studies

The capacitive behavior of an electrode material is generally characterized by cyclic voltammetry (CV). Fig. 4A shows the characteristic CV curves of the synthesized $Ni/Ni(OH)_2$ and $NiO/Ni(OH)_2$ NSs at a 5 mV s^{-1} scan rate in 1 M KOH aqueous solution. In the case of $Ni/Ni(OH)_2$, two anodic peaks were observed; one was related to the oxidation of β-$Ni(OH)_2$ to β-NiOOH and the other one was related to the phase transformation of α-$Ni(OH)_2$ to β-$Ni(OH)_2$. Because of their unstable nature in alkaline conditions, only one cathode peak was observed, which is due to the reduction of β-NiOOH to β-$Ni(OH)_2$ within the cathodic region.[49] The CV curves are comprised of strong redox peaks, suggesting that the capacitance characteristics are mainly controlled by faradaic redox reactions, which is very distinct from that of EDLCs that usually yield a CV curve close to an ideal rectangular shape. Reversible peaks are observed for the $Ni/Ni(OH)_2$ and $NiO/Ni(OH)_2$ NSs. Consequently, the CV curves demonstrate that the $Ni/Ni(OH)_2$ electrode exhibits much better electrochemical behavior in terms of specific capacitance than the $NiO/Ni(OH)_2$ electrode, owing to their high integral area. We calculated the specific capacitance values of both $Ni/Ni(OH)_2$ and $NiO/Ni(OH)_2$ from eqn (1), which are 536 and 440 F g^{-1} at 5 mV s^{-1}, respectively.

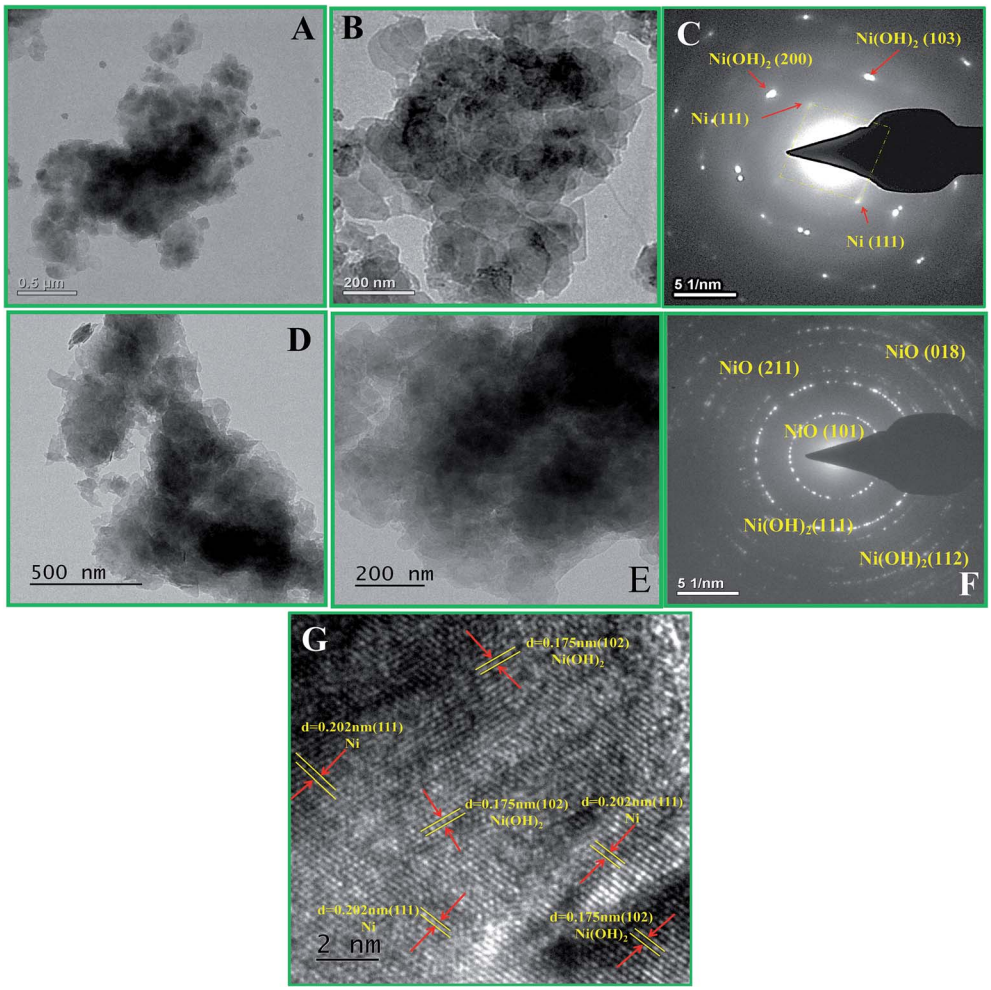

Fig. 3 (A and B) Transmission electron microscopic (TEM) images of Ni/Ni(OH)$_2$ NS at lower and higher magnification; (C) the corresponding SAED pattern; (D and E) TEM images of NiO/Ni(OH)$_2$ NS at lower and higher magnification; (F) the corresponding SAED pattern and (G) high resolution TEM image of Ni/Ni(OH)$_2$ NS.

Fig. 4B and S2A (ESI†) display the CV curves of Ni/Ni(OH)$_2$ and NiO/Ni(OH)$_2$ electrodes at various scan rates such as 5, 10, 25, 50, 75, 100, and 125 mV s^{-1}. It was observed that all the CV curves exhibited a similar pattern of anodic and cathodic peaks with increasing scan rates, demonstrating the good reversibility of the redox reaction at the nanostructure interface, with excellent rate capability. Moreover, the anodic and cathodic peaks were shifted towards the positive and negative potential with rising scan rates. This might be due to the diffusion effect of protons within the electrode or mass transfer limitations of electrolyte ions in order to neutralize the electronic charge on the electrode surface during the redox reaction.[50] From Fig. 4C, we can infer that the specific capacitance and the scan rate share an inverse relationship. This can be attributed to the circulation effect, which prevents the diffusion and movement of the electrolyte ions within the electrode at elevated scan rates, due to their inner active sites that are not capable of fully withstanding the redox alterations at higher scan rate.[51,52] Fig. 4D and S2B (ESI†) illustrate the changes in the specific capacitance of the Ni/Ni(OH)$_2$ and NiO/Ni(OH)$_2$ electrodes at different current densities (1–8 mA cm^{-2}). The symmetric and non-linear characteristics of the GCD curves are shown at various current densities, which further corroborate the pseudo-capacitive behavior of our working electrodes. The voltage plateaus in the charge/discharge process are consistent with faradaic oxidation and reduction peaks in the CV. For comparison, the GCD curves of both electrodes at current density of 1 mA cm^{-2} are shown in Fig. 5A. The calculated specific capacitance of the Ni/Ni(OH)$_2$ and NiO/Ni(OH)$_2$ electrodes are 450 and 343 F g^{-1}, respectively, at a current density of 1 mA cm^{-2}. For better understanding, we compared the capacitance of two composites Ni/Ni(OH)$_2$ and NiO/Ni(OH)$_2$ at various scan rates (5–125 mV s^{-1}) and at different current densities (1–8 mA cm^{-2}), tabulated as Tables S1 and S2,† respectively. From the tables, we can see that the Ni/Ni(OH)$_2$ NS composite shows better rate capability than the NiO/Ni(OH)$_2$ NS composite. Further, we calculated the coulombic efficiency (η) of the sample to check the reversibility of the working electrode, which was calculated by using the formula given below:

$$\eta = t_d/t_c \times 100 \quad (6)$$

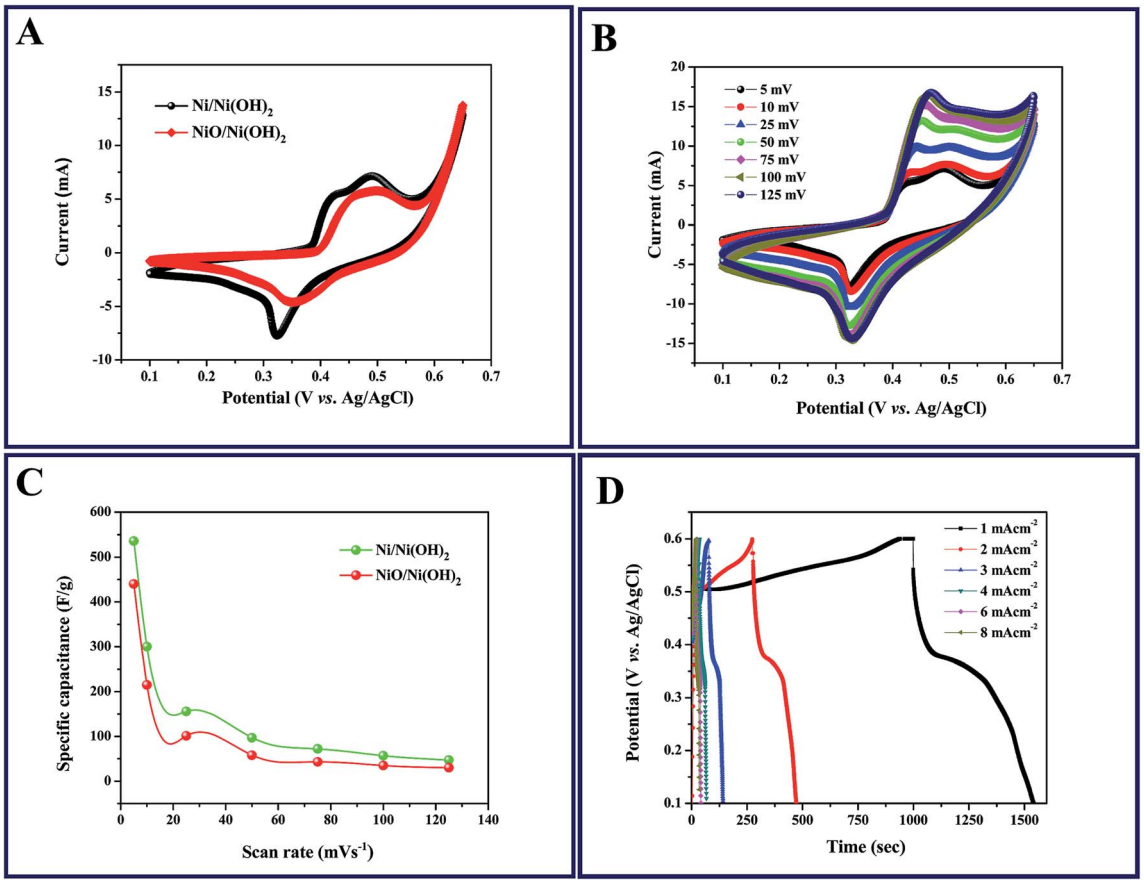

Fig. 4 (A) Cyclic voltammogram (CV) curves of $Ni/Ni(OH)_2$ and $NiO/Ni(OH)_2$ electrodes at 5 mV s^{-1}; (B) CV curves of the $Ni/Ni(OH)_2$ electrode at various scan rates; (C) specific capacitance as a function of scan rate for $Ni/Ni(OH)_2$ and $NiO/Ni(OH)_2$ electrodes; (D) galvanostatic charge/discharge (GCD) curves of $Ni/Ni(OH)_2$ at various current densities.

where t_d and t_c are discharge and charge times in seconds, respectively. The difference between them ($t_d - t_c$) indicates the kinetic irreversibility and coulombic efficiency. If the difference is lower, it means the working electrode has low kinetic irreversibility and high coulombic efficiency. In the case of $Ni/Ni(OH)_2$, we observed that the coulombic efficiency increased from 70 to ~100% for current densities from 1 to 8 mA cm^{-2}, respectively. At low current density, our working electrode shows low columbic efficiency, which might be due to the hierarchical nature of $Ni/Ni(OH)_2$ and physical triggering of the electrode material during charge discharge that is not so great, unlike at high current density. Previously, the same phenomena was observed by Pal *et al.* in the case of $CoSn(OH)_6$ nanostructures.[53] The high coulombic efficiency implies that our working electrode shows enhanced ionic diffusion. The charge-transfer resistance R_{CT} and ESR can be obtained from the Nyquist plots (Fig. 5B), fitted with an equivalent circuit, which is shown inset in Fig. 5B. It includes elements such as R_s, which represents the ESR at a point where the high frequency intercept on the real axis, R_{CT} is the charge transfer resistance, which is equivalent to the diameter of the semicircle, and Q is the constant phase element (CPE), due to the reduced semicircle and non-ideal capacitive behavior resulting from the heterogeneous nature of the electrodes.[54,55] The ESR of $Ni/Ni(OH)_2$ and $NiO/Ni(OH)_2$ NSs was measured to be 1.88 and 1.94 Ω, respectively, while the charge-transfer resistance R_{CT} was calculated to be 10.63, and 12.96 Ω, respectively. This clearly demonstrates the marginally higher conductive nature of $Ni/Ni(OH)_2$ over $NiO/Ni(OH)_2$. In addition, the charge-transfer resistance R_{CT}, also called the Faraday resistance, is a deterring factor for the specific power of the supercapacitor.[56] It is the low Faraday resistance that results in the high specific power of the $Ni/Ni(OH)_2$ NS electrode. Both $Ni/Ni(OH)_2$ and $NiO/Ni(OH)_2$ NSs show a slight difference in their R_{CT} and ESR values. Still, $Ni/Ni(OH)_2$ shows high specific capacitance and high rate capability at high current densities and scan rates than $NiO/Ni(OH)_2$, which implies that the Ni metal core in the $Ni/Ni(OH)_2$ composite plays a significant role in facilitating fast ion transport and charge transfer through the electrode material owing to its conductive nature. This is in accordance with the capacitance values that we observed from the CV and GCD results. Fig. 5C depicts the endurance test for the $Ni/Ni(OH)_2$ electrode by a long-term GCD process. Until 1000 cycles, there is no fading in capacitance; after 1000 cycles, the capacitance gradually fades and finally shows capacitance retention up to 90% at a current density of 15 mA cm^{-2} after 4000 cycles. The columbic efficiency retained by the working electrode is 85%, calculated using eqn (7) shown in Fig. S3.† Furthermore, the inset of

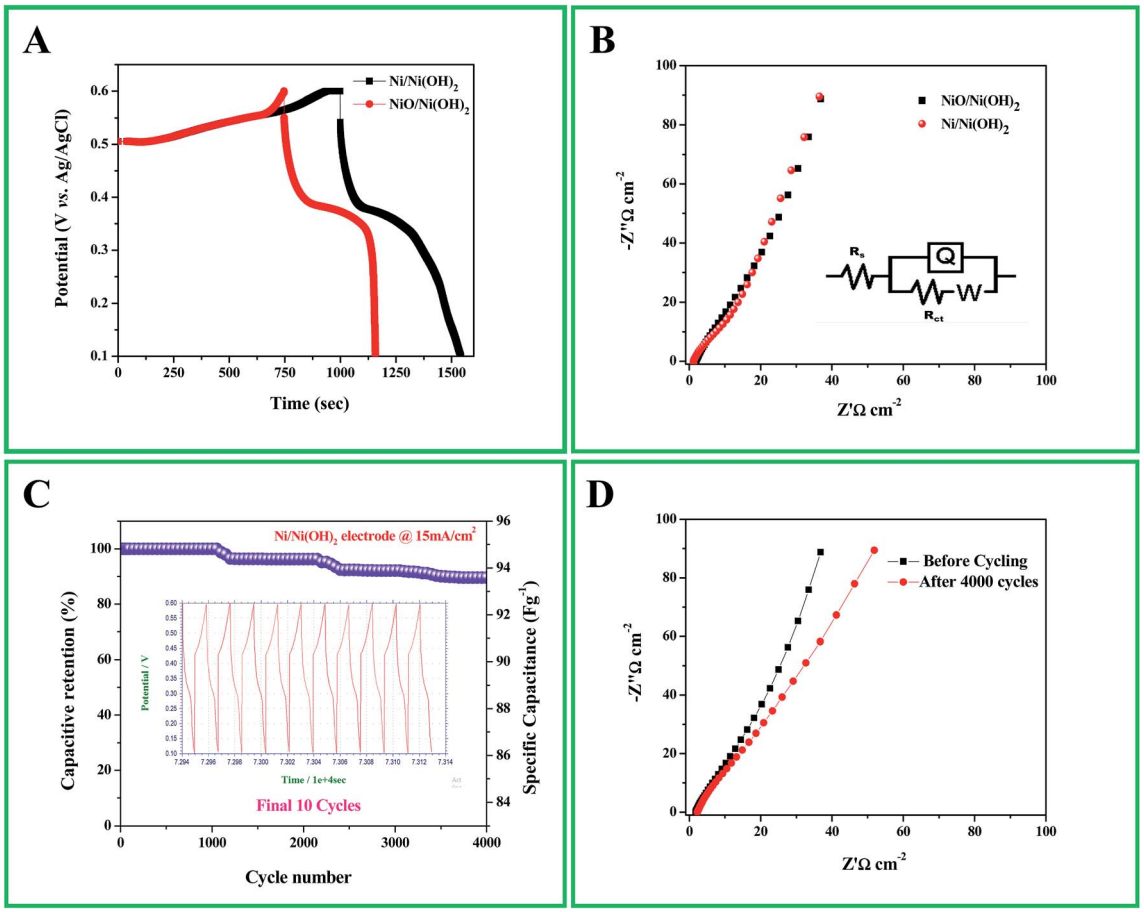

Fig. 5 (A) GCD curves of $Ni/Ni(OH)_2$ and $NiO/Ni(OH)_2$ electrodes at 1 mA cm^{-2} current density; (B) Nyquist plots of the $Ni/Ni(OH)_2$ and $NiO/Ni(OH)_2$ electrodes in the equivalent circuit; (C) cyclic performance of the $Ni/Ni(OH)_2$ electrode at 15 mA cm^{-2} for 4000 cycles, inset final 10 cycles; (D) Nyquist plots of the $Ni/Ni(OH)_2$ electrode before and after cycling.

Fig. 5C shows the final 10 charge discharge cycles, which implies that our active material is showing excellent rate capability. Fig. 5D depicts the EIS behavior of $Ni/Ni(OH)_2$ NS before and after cycling, fitted with the same equivalent circuit (inset of Fig. 5B). There is not much increase in ESR and R_{CT} values (before cycling 1.88 and 10.63 Ω and after cycling 2.89 and 13.84 Ω, respectively), which indicates the better electrochemical stability and excellent rate capability of $Ni/Ni(OH)_2$ NS. Of the two different NSs, $Ni/Ni(OH)_2$ shows better electrochemical performance compared to $NiO/Ni(OH)_2$. This is attributed to the nickel metal cores that are present in the $Ni/Ni(OH)_2$ NS, as well as the high specific surface area (SSA) of 58.13 m^2 g^{-1}, compared to the $NiO/Ni(OH)_2$ SSA of 27.26 m^2 g^{-1} using N_2 adsorption–desorption isotherms *via* the Brunauer–Emmett–Teller BET surface area measurement. Considering that the electrochemical performance of $Ni/Ni(OH)_2$ materials largely depends on their surface nano sheet structure and electronic conductivity, we propose three aspects that contribute to the superior electrochemical performance of the $Ni/Ni(OH)_2$ NSs. First, the specific surface area (SSA) of the as-synthesized $Ni/Ni(OH)_2$ NSs is higher than the $NiO/Ni(OH)_2$, consequently promoting the diffusion of electrolyte on the surface of the electrode and electrical conductivity of the electrode. Second, the presence of conductive Ni metal as part of the nano sheets will promote the electric conductivity of the electrode and thus, it provides a better way to produce commercial ASC cells because the electrode size is independent of the resistance, owing to the conductive nature of nickel metal. The third aspect relates to the clean and irregular structures. The disorder in $Ni/Ni(OH)_2$ can greatly improve electrochemical efficiency, and a low-crystalline material has the potential to exhibit excellent electrochemical performance because of its high structural disorder. Moreover, the $Ni/Ni(OH)_2$ NSs are well adapted to the surface of the nickel foam electrode. This adaptability not only maintains structural continuity, but also results in good electrical contact between the nano sheets and the electrode, which is vital for commendable electrochemical performance. Further, we proceeded to fabricate aqueous ASC, $Ni/Ni(OH)_2$ as positive electrode and activated carbon as the negative electrode, as discussed in detail in the following section.

Two electrode (ASC) electrochemical studies

The detailed electrochemical study on $Ni/Ni(OH)_2$ and $NiO/Ni(OH)_2$ NSs revealed the superior activity of $Ni/Ni(OH)_2$. By using activated carbon (AC) as the negative electrode, an ASC

with reasonable power and energy density can easily be fabricated along with our Ni/Ni(OH)$_2$ NS as a positive electrode, while eliminating the use of costly carbons (graphene, graphene oxides, *etc.*). The electrochemical performance of AC and Ni/Ni(OH)$_2$ NSs were examined separately by running CV at a 5 mV s^{-1} scan rate in 1 M KOH electrolyte (Fig. S4†). The rectangular shape of the CV acquired for AC without any redox peaks indicates the EDLC properties of AC, whereas the CV of Ni/Ni(OH)$_2$ does have a redox couple as expected, indicative of the pseudocapacitive behavior. From the careful evaluation of the obtained results on both Ni/Ni(OH)$_2$ and AC, the optimum voltage window was taken to be 1.65 V. The charge/discharge process of the ASC can be depicted as follows:

$$\beta\text{-Ni(OH)}_2 \rightleftharpoons \beta\text{-NiOOH} + \text{H}_2\text{O} + \text{e}^-$$

$$\text{C} + \text{KOH} \rightleftharpoons \text{CK}^+ + \text{OH}^-$$

The analysis of the specific capacitance values of Ni/Ni(OH)$_2$ and AC led to the optimal mass ratio of 1 : 4 in fabricating the ASC from eqn (6). The ASC cell was subjected to CV analysis in 1 M KOH solution at various scan rates ranging from 5–125 mV s^{-1} as shown in Fig. 6A. The shape of the CV curves looks slightly similar to that observed for the three electrode system of Ni/Ni(OH)$_2$ NSs. However, the combined effect of the EDLC properties from AC and redox characteristics from Ni/Ni(OH)$_2$ can be seen as the scan rate increases. It is noteworthy here that although Ni(OH)$_2$ is known for being a better oxygen evolving catalyst in alkaline solutions, with the optimized mass ratio taken for the fabrication of the asymmetric capacitor, no such gas evolution was witnessed within the potential window of 1.65 V. Fig. 6B illustrates the GCD plots at different current densities (2–20 mA cm^{-2}) with the potential window of 1.65 V. By making use of eqn (2), the maximum specific capacitance for the asymmetric device was achieved at current density of 2 mA cm^{-2} and found to be 62 F g^{-1}. We compared our results with other previous reports which are tabulated in Table 2.[7,18,56–61] From Table 2, we can see that our ASC is highly competitive with NiO//RGO, nitrogen doped graphene//$LiNi_{0.5}Mn_{1.5}O_4$ and AC//$V_2O_5 \cdot 0.6H_2O$ ASCs, and shows higher specific capacitance than most of the previous reports as tabulated. Further, we checked the columbic efficiency and kinetic irreversibility by making use

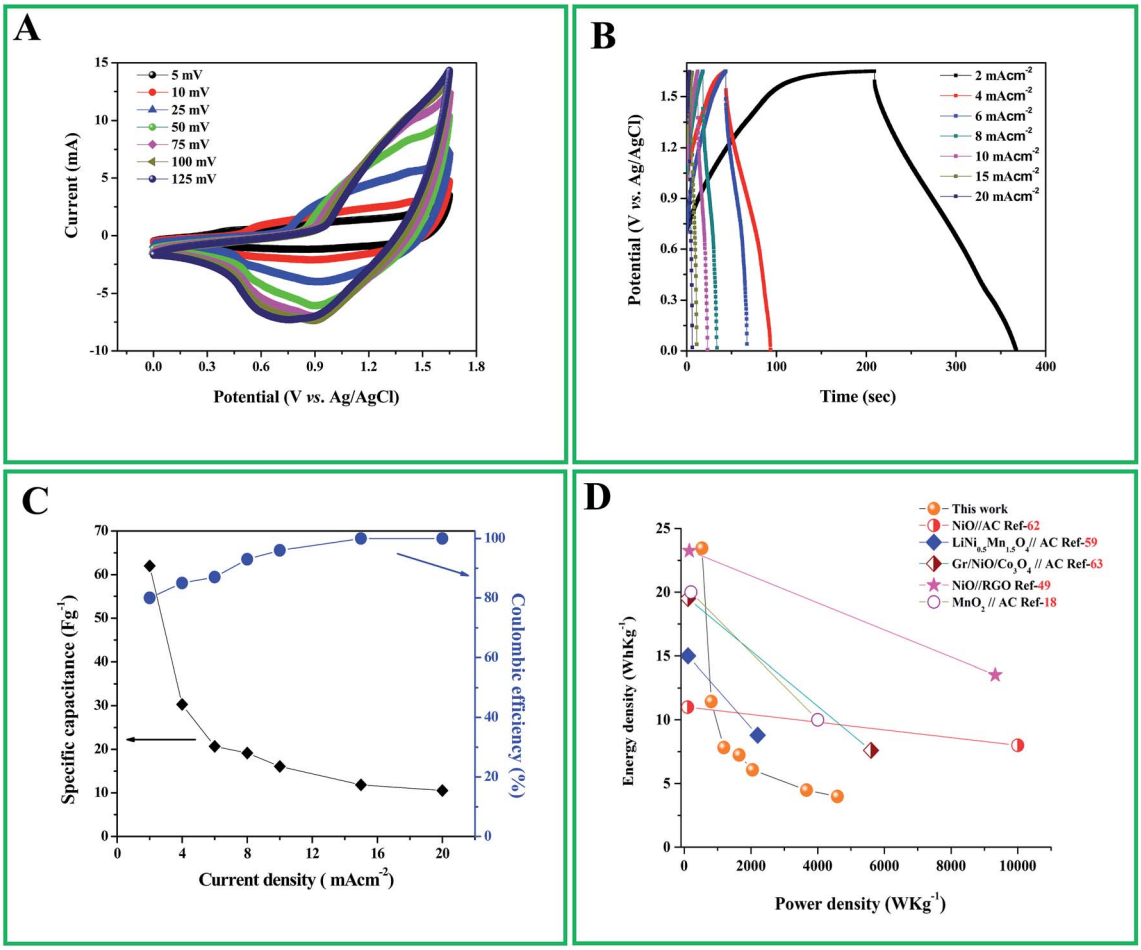

Fig. 6 (A) CV curves of ASC fabricated using Ni/Ni(OH)$_2$//AC at various scan rates; (B) galvanostatic charge/discharge (GCD) curves of ASC at various current densities. (C) Specific capacitance and coulombic efficiency as function of current density for ASC; (D) Ragone plot comparison with previous reports.

Table 2 Comparative specific capacitance of the Ni/Ni(OH)$_2$//AC ASC cell and other earlier reports

S. No.	Positive electrode	Negative electrode	Current density	Operational voltage	Specific capacitance (F g^{-1})	Reference
1	NiO	Reduced graphine oxide (RGO)	0.2 A g^{-1}	0–1.5	74.4	56
2	Activate carbon (AC)	MnO_2	29.8 mA h g^{-1}	0–2	53.7	57
3	Activate carbon (AC)	$V_2O_5 \cdot 0.6H_2O$	50.2 mA h g^{-1}	0–1.8	64.4	58
4	Nitrogen doped graphene	$LiNi_{0.5}Mn_{1.5}O_4$	0.5 mA cm^{-2}	0–1.3	72	59
5	MnO_2	AC	10 mA cm^{-2}	0–2.2	53	60
6	MnO_2/graphene	Graphene	0.5 A g^{-1}	0–2	31	7
7	MnO_2	AC	0.18 A g^{-1}	0–2.2	30	18
8	$LiMnSiO_4$/C	AC	1 mA cm^{-2}	0–3	43.2	61
9	**Ni/Ni(OH)$_2$ NS**	**AC**	**2 mA cm^{-2}**	**0–1.65**	**62**	**This work**

of eqn (7) for the current densities of 2 and 20 mA cm^{-2}, which we found to be 80% and 100%, respectively (Fig. 6C), and hence it can be inferred that at high current density, our ASC also shows high reversibility and enhanced rate capability. Fig. 6C illustrates the plot of specific capacitance with respect to the current densities and it dictates that as the current density increases from 2–20 mA cm^{-2}, the specific capacitance decreases, which is attributed to their inner active sites that are not capable of completely withstanding the redox alterations at higher scan rates.[51,52]

The power density (PD) and energy density (ED) are generally used as important parameters to characterize the electrochemical performance of electrochemical cells. The ED at different PD was calculated for our ASC from the discharge curves at different current densities according to eqn (3) and (4). The plot of energy density *versus* power density (Ragone plot) of the fabricated asymmetric cell was constructed from the GCD measurements carried out at various current densities from 2–20 mA cm^{-2} and was compared with previous ASC reports as shown in Fig. 6D. The ED and PD of our ASC are higher than the previous reports as observed in Fig. 6D.[18,49,59,62,63] Beyond the obvious reduction in the energy density upon increasing the power density, noticeable enhancements were noted in both. This might be due to the application of a comparatively high potential window of 0–1.65 V. The Ni/Ni(OH)$_2$//AC asymmetric cell exhibited good retention ability in energy density from 23.45 W h kg^{-1} to 3.9 W h kg^{-1}, while increasing the power density from 530 W kg^{-1} to 4598 W kg^{-1}. The observed energy density is higher than the energy density observed for symmetric capacitors made of AC and other expensive carbon materials such as CNT, graphene and porous graphene for which the observed energy densities were less than 10 W h kg^{-1}.[64–67] The enhanced cycling stability was noticed even after 6000 consecutive cycles of GCD at a current density of 15 mA cm^{-2} between 0 and 1.65 V. Fig. 7A shows the capacitance retention ratio of the asymmetric capacitor charged at 1.65 V as a function of the cycle number. It is worth noting that the specific capacitance sharply increases after 2000 cycles. A substantial increase in the specific capacitance while extending the cycling might be due to surface wetting. The highly improved chronic cycling stability is depicted through the impressive 90.6% retention of specific capacitance of our asymmetric cell, even after 6000 cycles. Initially, we observed a small decrease in capacitance in the range of 1000 to 2000 cycles, which might be due to some electro active material not being completely accessible for the diffusion of ions.[68,69] After continuous cycling, all the inactive parts of the working electrodes were completely open for diffusion of electrolyte ions and consequently, capacitance retention improved and showed the highest capacitance retention in the range of 3000–4000 cycles.[70] For better understanding the first 20 cycles, 20 cycles in the middle and the last 20 cycles are provided in Fig. S6 and S7,† respectively. The reversibility and the rate capability were determined by checking the CV profile after 6000 GCD cycles, shown in the inset of Fig. 7A. The two CV curves exhibit nearly similar profiles that imply better reversibility and excellent rate capability of our ASC cell. Further, we checked the columbic efficiency of the ASC cell during 6000 cycles. The columbic efficiency observed for the first cycle was 98%, and the efficiency retained after 6000 cycles was 90% (Fig. S5†). Moreover, the observed cycling stability and retention of specific capacitance is comparatively better than some previous reports of similar studies, such as $NiMn_2O_4$@CNT//AC showing 83% capacitance retention after 3000 cycles,[71] NiO//RGO with 88% retention after 2000 cycles,[56] NiCoS//AC showing 73.1% retention after 3000 cycles,[72] Ni(OH)$_2$/CNT//AC with 83% retention after 3000 cycles,[73] AC//AC–NiO NFs with 88% retention after 5000 cycles,[74] NiCoS//AC showing 79.1% retention after 6000 cycles,[75] and Ni(OH)$_2$/graphene//RuO_2/graphene with 92% retention after 5000 cycles.[76] Further, we carried out the EIS to find out the ESR and R_{CT} of the ASC cell before and after 6000 cycles. Fig. 7B shows Nyquist plots of the ASC cell before and after cycling, fitted with an equivalent circuit, as shown in the inset of Fig. 5B. A distorted semicircle in the high frequency region and a line with a slope in the low frequency region, are observed in the Nyquist plot. The semicircle signifies the charge transfer process and the slope indicates the capacitive nature of the ASC cell. The ESR of the ASC cell is not varied before and after cycling and remains at 1.14 ohm, but the R_{CT} increased from 0.61 to 0.87 ohm after cycling. This signifies the greater stability and high rate capability of the ASC cell. The synergism between the negative AC electrode and positive Ni/Ni(OH)$_2$ electrode along with the wide potential window has substantially increased the overall electrochemical performance of the

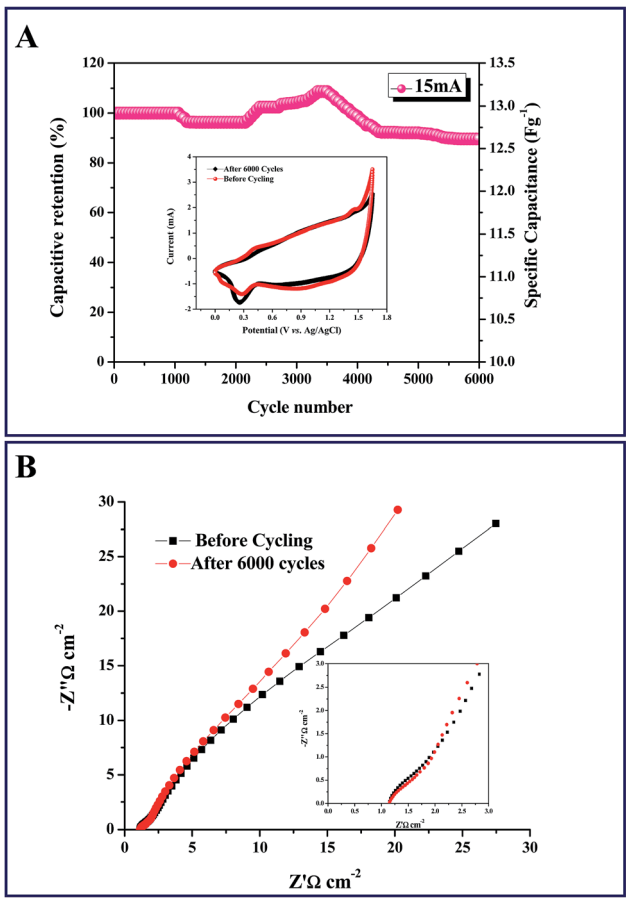

Fig. 7 (A) Cyclic performance of ASC at 15 mA cm^{-2} for 6000 cycles. Inset: CV curves at a scan rate of 5 mV s^{-1} before and after 6000 cycles. (B) Nyquist plots of the ASC cell before and after cycling; inset: high frequency region of Nyquist plot.

fabricated ASC cell ($Ni/Ni(OH)_2$//AC). Further, the ASC cell shows 90% of coulombic efficiency, even after 6000 cycles at high current density of 15 mA cm^{-2} (Fig. S5†), which can be attributed to the low ohmic resistance of the positive $Ni/Ni(OH)_2$ NS electrode, due to the presence of a conductive network of nickel metal. Moreover, it is advantageous to produce a commercial ASC cell because the electrode size is independent of the resistance, due to the conductive nature of nickel metal.[77–79] In the future, we hope that this will open up a new avenue for fabricating other transition metal oxide/hydroxide composites without using conductive substrates, for application in different areas such as lithium ion batteries, fuel cells and biosensors.

Conclusion

In summary, we have successfully synthesized $Ni/Ni(OH)_2$ and $NiO/Ni(OH)_2$ NSs using ethanol as a reducing agent in the presence of KOH, and studied their electrochemical properties in three and two electrode systems. In a three electrode system $Ni/Ni(OH)_2$ shows better electrochemical properties in terms of specific capacitance and conductive nature, compared to $NiO/Ni(OH)_2$ NSs. We have fabricated a hybrid supercapacitor using $Ni/Ni(OH)_2$ NSs and AC as the positive and negative electrodes, respectively. The ASC showed good specific capacitance, relatively high energy density, and a consistent cycling stability at an operating voltage of about 1.65 V in KOH aqueous electrolytes. It was found that coupling the $Ni/Ni(OH)_2$ NSs with AC to harvest supercapacitors yields a high specific capacitance of 62 F g^{-1} at a current density of 2 mA cm^{-2}. The systematic optimization of the mass of two electrodes resulted in the energy density of 23.45 W h kg^{-1} without sacrificing the power density. The galvanostatic charge–discharge experiment showed excellent capacitance retention of ~90%, even after 6000 consecutive cycles, which is a remarkable achievement for the field of ASCs. As a result of the interesting findings obtained in our detailed study on asymmetric $Ni/Ni(OH)_2$//AC supercapacitors, we state here that the $Ni/Ni(OH)_2$ NSs based ASCs could be the system of choice to meet the increasing demands for energy storage devices with high power and energy densities. The synthesis procedure can also be applied to other transition metals to synthesize their metal/metal hydroxide composites to enhance their conductive nature deprived of using conductive substrate.

Acknowledgements

Authors wish to acknowledge Dr Vijayamohan K. Pillai, Director, CSIR-CECRI and Dr M. Jayachandran, HOD, ECMS-Division, CSIR-CECRI for their continuous support and encouragement. The help extended by Dr B. Subramanian, Sr Scientist, ECMS-Division, during electrochemical measurements is kindly acknowledged. S. R. Ede and S. Anantharaj wish to acknowledge CSIR, New Delhi, India, for SRF fellowships. Help from Mr A. Rathishkumar (TEM in-charge) and central instrumentation facility (CIF), CSIR-CECRI, Karaikudi, Tamil Nadu, India, are acknowledged.

References

1 P. Simon and Y. Gogotsi, *Nat. Mater.*, 2008, **7**, 845.
2 B. E. Conway, *Electrochemical Supercapacitors: Scientific Fundamentals and Technological Applications*, 1999.
3 J. R. Miller and P. Simon, *Science*, 2008, **321**, 651.
4 R. Kötz, R. Kötz, M. Carlen and M. Carlen, *Electrochim. Acta*, 2000, **45**, 2483.
5 A. Burke, *Electrochim. Acta*, 2007, **53**, 1083.
6 A. Burke, *J. Power Sources*, 2000, **91**, 37.
7 Z. S. Wu, W. Ren, D. W. Wang, F. Li, B. Liu and H. M. Cheng, *ACS Nano*, 2010, **4**, 5835.
8 M. R. Lukatskaya, B. Dunn and Y. Gogotsi, *Nat. Commun.*, 2016, **7**, 1.
9 A. Izadi-Najafabadi, S. Yasuda, K. Kobashi, T. Yamada, D. N. Futaba, H. Hatori, M. Yumura, S. Iijima and K. Hata, *Adv. Mater.*, 2010, **22**, 235.
10 L. Demarconnay, E. Raymundo-Pinero and F. Beguin, *J. Power Sources*, 2011, **196**, 580.
11 W. G. Pell and B. E. Conway, *J. Power Sources*, 2004, **136**, 334.
12 T. Cottineau, M. Toupin, T. Delahaye, T. Brousse and D. Bélanger, *Appl. Phys. A: Mater. Sci. Process.*, 2006, **82**, 599.

13 J. Kim, C. Young, J. Lee, M.-S. Park, M. Shahabuddin, Y. Yamauchi and J. H. Kim, *Chem. Commun.*, 2016, **52**, 13016.
14 R. R. Salunkhe, J. Tang, N. Kobayashi, J. Kim, Y. Ide, S. Tominaka, J. H. Kim and Y. Yamauchi, *Chem. Sci.*, 2016, **7**, 5704.
15 Y. Wang, Z. Wang and Y. Xia, *Electrochim. Acta*, 2005, **50**, 5641.
16 M. S. Hong, S. H. Lee and S. W. Kim, *Electrochem. Solid-State Lett.*, 2002, **5**, A227.
17 T. Brousse, M. Toupin and D. Bélanger, *J. Electrochem. Soc.*, 2004, **151**, A614.
18 V. Khomenko, E. Raymundo-Piñero and F. Béguin, *J. Power Sources*, 2006, **153**, 183.
19 Y. Zhu, C. Cao, S. Tao, W. Chu, Z. Wu and Y. Li, *Sci. Rep.*, 2013, **4**, 1–7.
20 H. Wang, H. S. Casalongue, Y. Liang and H. Dai, *J. Am. Chem. Soc.*, 2010, **132**, 7472.
21 S. R. Ede, A. Ramadoss, S. Anantharaj, U. Nithiyanantham and S. Kundu, *Phys. Chem. Chem. Phys.*, 2014, **16**, 21846.
22 B. Saravanakumar, K. K. Purushothaman and G. Muralidharan, *ACS Appl. Mater. Interfaces*, 2012, **4**, 4484.
23 C. Zheng, C. Cao, Z. Ali and J. Hou, *J. Mater. Chem. A*, 2014, 16467.
24 G. Binitha, M. S. Soumya, A. A. Madhavan, P. Praveen, A. Balakrishnan, K. R. V Subramanian, M. V. Reddy, S. V. Nair, A. S. Nair and N. Sivakumar, *J. Mater. Chem. A*, 2013, 11698.
25 U. Nithiyanantham, S. R. Ede, T. Kesavan, P. Ragupathy, M. D. Mukadam, S. M. Yusuf and S. Kundu, *RSC Adv.*, 2014, **4**, 38169.
26 U. Nithiyanantham, S. R. Ede, S. Anantharaj and S. Kundu, *Cryst. Growth Des.*, 2015, **2**, 673.
27 S. R. Ede, A. Ramadoss, U. Nithiyanantham, S. Anantharaj and S. Kundu, *Inorg. Chem.*, 2015, 3851.
28 L. L. Kong, C. Zhang, S. Zhang, J. Wang, R. Cai, C. Lv, W. Qiao, L. Ling and D. Long, *J. Mater. Chem. A*, 2014, 17962.
29 Z. Liang, Y. Zhu and X. Hu, *J. Phys. Chem. B*, 2004, **108**, 3488.
30 M. Yu, J. Chen, J. Liu, S. Li, Y. Ma, J. Zhang and J. An, *Electrochim. Acta*, 2015, **151**, 99.
31 C.-L. Ho and M.-S. Wu, *J. Phys. Chem. C*, 2011, **115**, 22068.
32 X. Gong, J. P. Cheng, F. Liu, L. Zhang and X. Zhang, *J. Power Sources*, 2014, **267**, 610.
33 C. Guan, J. Liu, C. Cheng, H. Li, X. Li, W. Zhou, H. Zhang and H. J. Fan, *Energy Environ. Sci.*, 2011, 4496.
34 D.-H. Chen and S.-H. Wu, *Chem. Mater.*, 2000, **12**, 1354.
35 A. P. Grosvenor, M. C. Biesinger, R. S. C. Smart and N. S. Mcintyre, *Surf. Sci.*, 2006, **600**, 1771.
36 G.-F. Chen, X.-X. Li, L.-Y. Zhang, N. Li, T. Y. Ma and Z.-Q. Liu, *Adv. Mater.*, 2016, **28**, 7680.
37 K. Xiao, J.-W. Li, G.-F. Chen, Z.-Q. Liu, N. Li and Y.-Z. Su, *Electrochim. Acta*, 2014, **149**, 341.
38 G.-F. Chen, Y.-Z. Su, P.-Y. Kuang, Z.-Q. Liu, D.-Y. Chen, X. Wu, N. Li and S.-Z. Qiao, *Chem.–Eur. J.*, 2015, **21**, 4614.
39 Z.-Q. Liu, G.-F. Chen, P.-L. Zhou, N. Li and Y.-Z. Su, *J. Power Sources*, 2016, **317**, 1.
40 S.-H. Wu and D.-H. Chen, *J. Colloid Interface Sci.*, 2003, **259**, 282.
41 N. R. N. Roselina, A. Azizan, K. M. Hyie, A. Jumahat and M. A. A. Bakar, *Procedia Engineering*, 2013, **68**, 43.
42 M. G. Rosmaninho, F. C. C. Moura, L. R. Souza, R. K. Nogueira, G. M. Gomes, J. S. Nascimento, M. C. Pereira, J. D. Fabris, J. D. Ardisson, M. S. Nazzarro, K. Sapag, M. H. Araujo and R. M. Lago, *Appl. Catal., B*, 2012, **115**, 45.
43 A. Pal and T. Pal, *J. Raman Spectrosc.*, 1999, **204**, 199.
44 S. Kundu, D. Huitink, K. Wang and H. Liang, *J. Colloid Interface Sci.*, 2010, **344**, 334.
45 S. R. Ede, U. Nithiyanantham and S. Kundu, *Phys. Chem. Chem. Phys.*, 2014, **16**, 22723.
46 S. Ayyappan, R. S. Gopalan, G. N. Subbanna and C. N. R. Rao, *J. Mater. Res.*, 1997, **12**, 398.
47 A. Pal, S. Shah and S. Devi, *Mater. Chem. Phys.*, 2009, **114**, 530.
48 U. Nithiyanantham, S. R. Ede and S. Kundu, *J. Mater. Chem. C*, 2014, **2**, 3782.
49 J. M. Skowronski and A. Wazny, *J. New Mater. Electrochem. Syst.*, 2006, **9**, 345.
50 H. Jiang, T. Zhao, C. Li and J. Ma, *J. Mater. Chem.*, 2011, **21**, 3818.
51 U. M. Patil, K. V. Gurav, V. J. Fulari, C. D. Lokhande and O. Shim, *J. Power Sources*, 2009, **188**, 338.
52 J. Lang, L. Kong, W. Wu, Y. Luo and L. Kang, *Chem. Commun.*, 2008, 4213.
53 R. Sahoo, A. K. Sasmal, C. Ray, S. Dutta, A. Pal and T. Pal, *ACS Appl. Mater. Interfaces*, 2016, **8**, 17987.
54 X. Dominguez-Benetton, S. Sevda, K. Vanbroekhoven and D. Pant, *Chem. Soc. Rev.*, 2012, **41**, 7228.
55 J. Jorcin, M. E. Orazem, P. Nadine and B. Tribollet, *Electrochim. Acta*, 2006, **51**, 1473.
56 X. Ren, C. Guo, L. Xu, T. Li, L. Hou and Y. Wei, *ACS Appl. Mater. Interfaces*, 2015, **7**, 19930.
57 Q. Qu, P. Zhang, B. Wang, Y. Chen, S. Tian, Y. Wu and R. Holze, *J. Phys. Chem. C*, 2009, **113**, 14020.
58 Q. T. Qua, Y. Shi, L. L. Li, W. L. Guo, Y. P. Wua, H. P. Zhang, S. Y. Guan and R. Holze, *Electrochem. Commun.*, 2009, **11**, 1325.
59 R. Aswathy, T. Kesavan, K. T. Kumaran and P. Ragupathy, *J. Mater. Chem. A*, 2015, **3**, 12386.
60 Y. Xue, Y. Chen, M.-L. Zhang and Y.-D. Yan, *Mater. Lett.*, 2008, **62**, 3884.
61 K. Karthikeyan, V. Aravindan, S. B. Lee, I. C. Jang, H. H. Lim, G. J. Park, M. Yoshio and Y. S. Lee, *J. Power Sources*, 2010, **195**, 3761.
62 D.-W. Wang, F. Li and H.-M. Cheng, *J. Power Sources*, 2008, **185**, 1563.
63 H. Wang, C. M. B. Holt, Z. Li, X. Tan, B. S. Amirkhiz, D. M. Xu, Z. Xu, B. C. Olsen and T. Stephenson, *Nano Res.*, 2012, **5**, 605.
64 Z. Fan, J. Yan, T. Wei, L. Zhi, G. Ning, T. Li and F. Wei, *Adv. Funct. Mater.*, 2011, **21**, 2366.
65 Z. Chen, V. Augustyn, J. Wen, Y. Zhang, M. Shen, B. Dunn and Y. Lu, *Adv. Mater.*, 2011, **23**, 791.
66 D. W. Wang, F. Li, M. Liu, G. Q. Lu and H. M. Cheng, *Angew. Chem., Int. Ed.*, 2008, **47**, 373.

67 Q. Qu, L. Li, S. Tian, W. Guo, Y. Wu and R. Holze, *J. Power Sources*, 2010, **195**, 2789.
68 Z. Gao, J. Wang, Z. Li, W. Yang, B. Wang, M. Hou, Y. He, Q. Liu, T. Mann, P. Yang, M. Zhang and L. Liu, *Chem. Mater.*, 2011, **23**, 3509.
69 H. Sun, L. Cao and L. Lu, *Energy Environ. Sci.*, 2012, **5**, 6206.
70 X. Xia, J. Tu, Y. Zhang, X. Wang, C. Gu and H. J. Fan, *ACS Nano*, 2012, **6**, 5531.
71 H. Nan, W. Ma, Z. Gu, B. Geng and X. Zhang, *RSC Adv.*, 2015, **5**, 24607.
72 Y. Li, L. Cao, L. Qiao, M. Zhou, Y. Yang, P. Xiao and Y. Zhang, *J. Mater. Chem. A*, 2014, **2**, 6540.
73 Z. Tang, C. Tang and H. Gong, *Adv. Funct. Mater.*, 2012, **22**, 1272.
74 M. S. Kolathodi, M. Palei and T. S. Natarajan, *J. Mater. Chem. A*, 2015, **3**, 7513.
75 X. Li, Q. Li, Y. Wu, M. Rui and H. Zeng, *ACS Appl. Mater. Interfaces*, 2015, **7**, 19316.
76 H. Wang, Y. Liang, T. Mirfakhrai, Z. Chen, H. S. Casalongue and H. Dai, *Nano Res.*, 2011, **4**, 729.
77 Q. Lu, M. W. Lattanzi, Y. Chen, X. Kou, W. Li, X. Fan, K. M. Unruh, J. G. Chen and J. Q. Xiao, *Angew. Chem., Int. Ed.*, 2011, **50**, 6847.
78 G.-F. Chen, Z.-Q. Liu, J.-M. Lin, N. Li and Y.-Z. Su, *J. Power Sources*, 2015, **283**, 484.
79 Y.-Z. Su, K. Xiao, N. Li, Z.-Q. Liu and S.-Z. Qiao, *J. Mater. Chem. A*, 2014, **2**, 13845.